Advanced Fiber Materials (2022) 4:487–502
https://doi.org/10.1007/s42765-021-00123-6

RESEARCH ARTICLE

Tailored Carrier Transport Path by Interpenetrating Networks in Cathode Composite for High Performance All-Solid-State Li-SeS_2 Batteries

Lei Zhou[1] · Muhammad Khurram Tufail[1] · Yaozu Liao[2] · Niaz Ahmad[1] · Peiwen Yu[1] · Tinglu Song[5] · Renjie Chen[3,4] · Wen Yang[1]

Received: 31 August 2021 / Accepted: 30 November 2021 / Published online: 9 February 2022

Abstract

All-solid-state Li-SeS_2 batteries (ASSLSs) are more attractive than traditional liquid Li-ion batteries due to superior thermal stability and higher energy density. However, various factors limit the practical application of all-solid-state Li-SeS_2 batteries, such as the low ionic conductivity of the solid-state electrolyte and the poor kinetic property of the cathode composite, resulting in unsatisfactory rate capability. Here, we employed a traditional ball milling method to design a $Li_7P_{2.9}W_{0.05}S_{10.85}$ glass–ceramic electrolyte with high conductivity of 2.0 mS cm^{-1} at room temperature. In order to improve the kinetic property, an interpenetrating network strategy is proposed for rational cathode composite design. Significantly, the disordered cathode composite with an interpenetrating network could promote electronic and ionic conduction and intimate contacts between the electrolyte–electrode particles. Moreover, the tortuosity factor of the carrier transport channel is considerably reduced in electrode architectures, leading to superior kinetic performance. Thus, assembled ASSLS exhibited higher capacity and better rate capability than its counterpart. This work demonstrates that an interpenetrating network is essential for improving carrier transport in cathode composite for high rate all-solid-state Li-SeS_2 batteries.

Keywords All-Solid-State Li-SeS_2 batteries · Tortuosity factors · Carrier transport · Cathode composite · Interpenetrating network

Introduction

Li-SeS_2 batteries are attracting marvelous research interest for electric vehicles and large-scale energy storage in the future due to their lower cost and higher energy density than the traditional lithium-ion battery [1–5]. SeS_2 has the advantage of having a high gravimetric capacity of 1124 mAh g^{-1}; it exists as an eight-membered ring molecule with Se-S bonds and is being explored as a cathode material due to Se (10^{-5} S cm^{-1}) better electric conductivity than S (10^{-30} S cm^{-1}) [6–9]. At the same time, Li_2Se demonstrated identical chemical properties and larger Li-ion migration ability than Li_2S [10, 11]. Moreover, it's possible that using

Lei Zhou and Muhammad Khurram Tufail contributed equally to this work.

✉ Renjie Chen
chenrj@bit.edu.cn

✉ Wen Yang
wenyang@bit.edu.cn

[1] Key Laboratory of Cluster Science of Ministry of Education, Beijing Key Laboratory of Photoelectronic/Electrophotonic Conversion Materials, School of Chemistry and Chemical Engineering, Beijing Institute of Technology, Beijing 100081, People's Republic of China

[2] State Key Laboratory for Modification of Chemical Fibers and Polymer Materials, College of Materials Science and Engineering, Donghua University, Shanghai 201620, People's Republic of China

[3] School of Material Science and Engineering, Beijing Institute of Technology, Beijing 100081, People's Republic of China

[4] Advance Technology Research Institute, Beijing Institute of Technology, Jinan 250300, People's Republic of China

[5] Experimental Center of Advanced Materials School of Materials Science and Engineering, Beijing Institute of Technology, Beijing 100081, People's Republic of China

Se instead of S in the cathode composite will result in superior active materials consumption and rate capability.

The employment of solid-state electrolytes (SSEs) in Li-SeS_2 batteries is supposed to alleviate liquid battery safety problems and the shuttling effect [12–16]. Sulfide-based electrolytes have a higher ionic conductivity advantage over other solid electrolyte classes [17, 18]. However, all-solid-state Li-SeS_2 batteries have poor rate capability, owing to non-ideal carrier transportation inside cathode composites and poor kinetic characteristics. Exceeding the limits necessitates developing new electrode materials and electrode architectures capable of eliciting chemistries for outstanding rate performance and high columbic efficiency. These materials must also be enriched with ionic and electronic conducting networks at the electrode level and optimized transportation parameters to improve electrode kinetics. Also, the efficient carrier migration, i.e., the ionic and electronic conduction within cathode composites, is still a challenge due to its complex microstructure and three components (electrolyte, active material, and conductive agent). The ideal composite cathode provides sufficient charge transport paths for electrons and Li-ions and restricted use of electronic insulating components and tailored transportation parameters. Also, in-depth knowledge of the kinetics of cathode composites in ASSLSs is still indistinct.

The high content of carbon-based materials (CNT, Super P, and VGCF) are consistently implemented in the cathode composites to enhance the kinetic performance of all-solid-state lithium batteries (ASSLBs) [19–22]. However, the inclusion of carbon conductive agents would severely degrade sulfide-based solid-state electrolytes and lead to the poor efficiency of ASSLBs. Meanwhile, incorporating conductive polymers into the cathode composites would lead to large voltage polarization in the cell due to interfacial side reactions between the conductive polymer and sulfide electrolytes [23, 24]. Moreover, the practical applications of ASSLSs are achieved by increasing the areal loading of cathode materials and decreasing the volume fractions of inactive components such as conductive agents [25]. Thus, the electrode architectures and their related tortuosity factors within the cathode composite significantly impact the electrochemical performance of ASSLBs.

Herein, $Li_7P_{2.9}W_{0.05}S_{10.85}$ glass–ceramic electrolyte with high lithium-ion conductivity is successfully synthesized by traditional ball milling and heat treatment. The carrier transport properties of cathode composites are well studied in ASSLSs. More important, an interpenetrating network is designed in cathode composite based on VGCF conductive agent. The interpenetrating network builds the low tortuosity of electrode architecture as well as enhances the cathode composites of electronic/ionic conduction. The assembled all-solid-state Li-SeS_2 batteries based on interpenetrating network cathode composite exhibit a high specific capacity of 512 mAh g^{-1} at the current density of 0.06 mA cm^{-1}. Surprisingly, it retains a reversible specific capacity of 506 mAh g^{-1} with 98.8% capacity retention after the 90th cycle. Besides, it also presents discharge capacities of 515, 430, 364, 329, 307 and 285 mAh g^{-1} at the current density of 0.06, 0.09, 0.12, 0.15, 0.18 and 0.21 mA cm^{-1}, respectively. As a result, the designed all-solid-state Li-SeS_2 battery demonstrates superior cycling stability and better rate capability.

Results and Discussion

$Li_7P_3S_{11}$, $Li_7P_{2.9}W_{0.05}S_{10.85,}$ and $Li_7P_{2.8}W_{0.1}S_{10.7}$ glass–ceramic electrolytes are prepared by traditional ball milling method and following crystallization process. Figure S1 displays the XRD pattern of $Li_7P_3S_{11}$, $Li_7P_{2.9}W_{0.05}S_{10.85,}$ and $Li_7P_{2.8}W_{0.1}S_{10.7}$ glass, obtained via high energy ball-milling. No diffraction peaks are displayed in Figure S1, showing that a glassy phase is generated after the ball milling process. Thus, high-quality glass–ceramic electrolytes could be obtained by precipitation of glass samples using high-temperature processing. Figure 1a presents the differential thermal analysis (DTA) curves of $Li_7P_3S_{11}$, $Li_7P_{2.9}W_{0.05}S_{10.85,}$ and $Li_7P_{2.8}W_{0.1}S_{10.7}$ glass samples. These DTA curves exhibited the same characteristics and a strong peak between 260 and 280 °C, corresponding to the exothermic effect of crystal growth [26, 27]. In order to attain the crystallization of $Li_7P_3S_{11}$, $Li_7P_{2.9}W_{0.05}S_{10.85,}$ and $Li_7P_{2.8}W_{0.1}S_{10.7}$ glass electrolytes more sufficiently, the temperature at the exothermic peak is chosen as the optimal condition. As a result, the glass electrolyte's heat treatment temperature is set to 270 °C. After appropriate heat treatment, the $Li_7P_3S_{11}$, $Li_7P_{2.9}W_{0.05}S_{10.85,}$ and $Li_7P_{2.8}W_{0.1}S_{10.7}$ glass–ceramic electrolytes were obtained successfully. The X-ray diffraction (XRD) technique is performed to analyze further the glass–ceramic electrolyte of phase and crystal structure. Figure 1b is the XRD pattern of the $Li_7P_3S_{11}$, $Li_7P_{2.9}W_{0.05}S_{10.85,}$ and $Li_7P_{2.8}W_{0.1}S_{10.7}$ glass–ceramic electrolytes. As shown in Fig. 1b, the characteristic peak of $Li_7P_{2.9}W_{0.05}S_{10.85}$ and $Li_7P_{2.8}W_{0.1}S_{10.7}$ glass–ceramic are identical to $Li_7P_3S_{11}$ glass–ceramics sample, indicating that $Li_7P_{2.9}W_{0.05}S_{10.85}$ and $Li_7P_{2.8}W_{0.1}S_{10.7}$ glass–ceramics deliver a similar $Li_7P_3S_{11}$ fast ionic conductor [28]. It is worth noting that the characteristic peak of $Li_7P_{2.9}W_{0.05}S_{10.85}$ and $Li_7P_{2.8}W_{0.1}S_{10.7}$ have slightly deviated under the basis in comparison to $Li_7P_3S_{11}$glass ceramics. The differences at marked (Fig. 1b) and magnified zone (Figure S2) suggest that W has been successfully doped into the glass–ceramic matrix of $Li_7P_3S_{11}$ after high-energy ball milling and heat treatment. Moreover, the minor deviation of the characteristic peak of $Li_7P_{2.9}W_{0.05}S_{10.85}$ and $Li_7P_{2.8}W_{0.1}S_{10.7}$ samples is

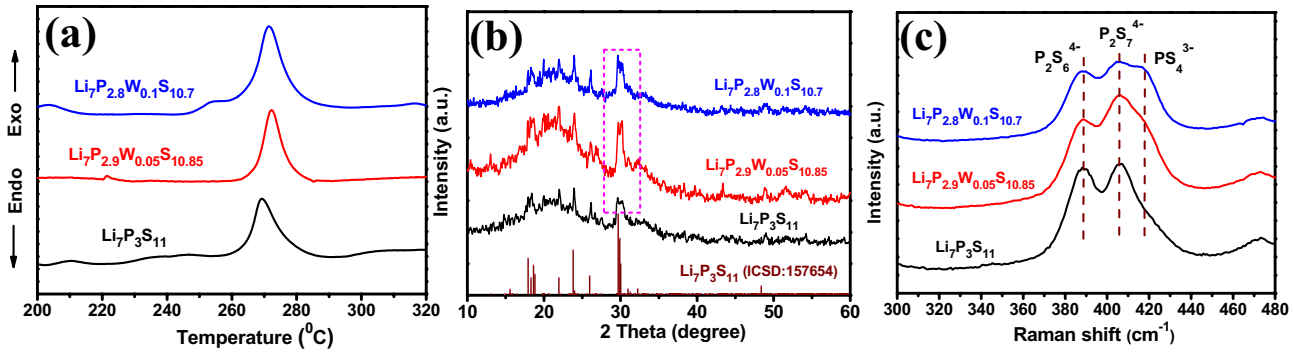

Fig. 1 **a** DTA curve for $Li_7P_3S_{11}$, $Li_7P_{2.9}W_{0.05}S_{10.85}$ and $Li_7P_{2.8}W_{0.1}S_{10.7}$ glass sample in argon atmosphere, **b** XRD pattern of $Li_7P_3S_{11}$, $Li_7P_{2.9}W_{0.05}S_{10.85}$ and $Li_7P_{2.8}W_{0.1}S_{10.7}$ glass–ceramic sample, **c** Raman spectra of $Li_7P_3S_{11}$, $Li_7P_{2.9}W_{0.05}S_{10.85}$ and $Li_7P_{2.8}W_{0.1}S_{10.7}$ glass–ceramic sample

due to W doping into $Li_7P_3S_{11}$-type electrolyte, generating lattice distortion.

Three peaks are detected at 417, 406, and 387 cm^{-1}, which belong to the stretching vibration of the P-S bonds in PS_4^{3-}, $P_2S_7^{4-}$ and $P_2S_6^{4-}$ conductive units, respectively as presents in Fig. 1c. Thus, the heteroatom doping pattern does not generate any new structural moieties in $Li_7P_3S_{11}$-type glass–ceramic electrolytes. Nonetheless, the relative peak intensity of the $P_2S_7^{4-}$ the conductive unit of $Li_7P_{2.9}W_{0.05}S_{10.85}$ sample is a little higher as compared to $Li_7P_3S_{11}$ and $Li_7P_{2.8}W_{0.1}S_{10.7}$ glass–ceramic samples. A small amount of the $P_2S_6^{4-}$ (less ionic conductive) units exist in the $Li_7P_{2.9}W_{0.05}S_{10.85}$ as compared to other glass–ceramic samples. The results deliver appropriate W doping tend to form additional $P_2S_7^{4-}$ (higher ionic conductive) units. Moreover, the $P_2S_7^{4-}$ ions contribute to improving ionic conductivity [29]. It is demonstrated that as-prepared $Li_7P_{2.9}W_{0.05}S_{10.85}$ glass–ceramic sample would present the highest ionic conductivity among other samples.

XPS technique is used to explore chemical elements and structure for the $Li_7P_{2.9}W_{0.05}S_{10.85}$ glass–ceramic electrolyte. Figure S3a reveals all existent elements and their valence states found in the $Li_7P_{2.9}W_{0.05}S_{10.85}$ sample and Figure S3b displays the XPS spectrum of S 2p. According to spin-orbital splitting, the S 2p peaks spectrum has two components, which could be assigned to S $2p_{3/2}$ and S $2p_{1/2}$. Furthermore, the Lorentzian-Gaussian function fits S 2p spectrum into different peaks. The coexistence of non-bridging sulfur bond (P-S-Li) and bridging sulfur bond (P-S-P) are evidenced by the presence of a peak at 161 eV and 163 eV, respectively [30]. Meanwhile, the peak of S $2p_{3/2}$ at 162 eV is ascribed to the double phosphorus-sulfur bond of P = S. Besides, the fitting peak at 162 eV also involves the W-S bond, indicating that W atoms successfully doped into the $Li_7P_3S_{11}$ crystal [31].

Figure 2a shows the EIS spectra of the as-prepared $Li_7P_3S_{11}$, $Li_7P_{2.9}W_{0.05}S_{10.85,}$ and $Li_7P_{2.8}W_{0.1}S_{10.7}$ glass–ceramic electrolytes at room temperatures. The resistance could be determined using the intersection coordinates of the EIS spectrum line and the horizontal axis. The resistance of $Li_7P_3S_{11}$, $Li_7P_{2.9}W_{0.05}S_{10.85,}$ and $Li_7P_{2.8}W_{0.1}S_{10.7}$ glass–ceramic electrolytes are 50, 35, and 62 Ω, respectively. The ionic conductivity ($б_{ion}$) of sulfide-based electrolyte is obtained from the thickness, area, and resistance of the sample according to the following Eq. (1):

$$б_{ion} = \frac{d}{A \cdot R} \tag{1}$$

where d presents the sample thickness, A is the sample area, and R is sample resistance at room temperature. Figure 2b exhibits that the ionic conductivity of $Li_7P_3S_{11}$, $Li_7P_{2.9}W_{0.05}S_{10.85,}$ and $Li_7P_{2.8}W_{0.1}S_{10.7}$ glass–ceramic electrolytes are 1.4, 2.0, and 1.1 mS cm^{-1}, respectively. The ionic conductivity of $Li_7P_{2.9}W_{0.05}S_{10.85}$ is higher than the previously reported sulfide electrolytes [32, 33]. According to the doping mechanism, the larger ionic radius of W would widen the lithium-ion channel and reduce the activation energy of the lithium-ion transition. As a result, the W-doped strategy contributes to improving the conduction of lithium-ion in the lattice distortion.

Activation energy is the most critical parameter to evaluate sulfide solid-state electrolyte performance. The activation energy (E_a) of sulfide electrolyte is calculated by Arrhenius Eq. (2):

$$б_{\text{ion}} = б_0 \ \exp\left(\frac{-E_a}{\text{RT}}\right) \tag{2}$$

where R denotes the gas constant, T is the absolute temperature, $б_0$ is the pre-exponential factor, and $б$ is the ionic conductivity. Figure 2c depicts a relationship between temperature and ionic conductivity that follows the Arrhenius formula. Thus, the activation energies of $Li_7P_3S_{11}$, $Li_7P_{2.9}W_{0.05}S_{10.85,}$ and $Li_7P_{2.8}W_{0.1}S_{10.7}$ glass–ceramic electrolytes are calculated to be 25.8, 23.2, and 26.6 kJ mol^{-1},

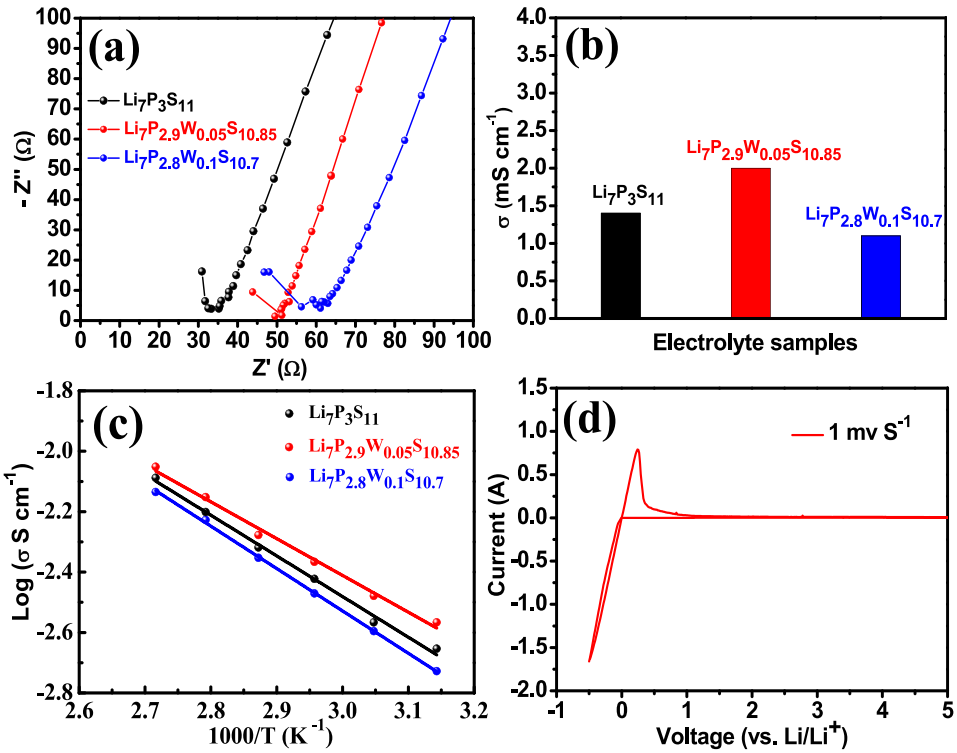

Fig. 2 **a** The impedance spectra of $Li_7P_3S_{11}$, $Li_7P_{2.9}W_{0.05}S_{10.85}$, and $Li_7P_{2.8}W_{0.1}S_{10.7}$ glass–ceramic electrolytes at room temperature, **b** the lithium-ion conductivities of $Li_7P_3S_{11}$, $Li_7P_{2.9}W_{0.05}S_{10.85}$ and $Li_7P_{2.8}W_{0.1}S_{10.7}$ glass–ceramic electrolytes, **c** Arrhenius plots of $Li_7P_3S_{11}$, $Li_7P_{2.9}W_{0.05}S_{10.85}$, and $Li_7P_{2.8}W_{0.1}S_{10.7}$ glass–ceramic electrolyte, **d** electrochemical stability window of $Li_7P_{2.9}W_{0.05}S_{10.85}$ glass–ceramic electrolyte

respectively. The results indicate that appropriate doping with aliovalent ions would reduce the activation energy and promotes fast transport of carrier in an inorganic conductor system.

In order to measure the electrochemical stability of $Li_7P_{2.9}W_{0.05}S_{10.85}$ glass–ceramic electrolyte, the non-blocking cell is constructed with lithium as a reference electrode and stainless steel (SS) as a working electrode in the glove box. The Li/$Li_7P_{2.9}W_{0.05}S_{10.85}$/SS cell is tested for CV with a scan rate of 1 mV S^{-1}. As revealed in Fig. 2d, the whole scanning potential range is from − 0.5 to 5 V. Except for lithium deposition peak ($Li^+ + e^- \rightarrow Li$) and lithium dissolution peak ($Li \rightarrow Li^+ + e^-$), no other peaks are observed, indicating that no side reactions occurred [34, 35]. Thus, the $Li_7P_{2.9}W_{0.05}S_{10.85}$ glass–ceramic electrolyte with lithium metal has good stability and an electrochemical window of up to 5 V.

Figure 3a displays ^{7}Li MAS NMR spectra of $Li_7P_3S_{11}$, $Li_7P_{2.9}W_{0.05}S_{10.85}$, and $Li_7P_{2.8}W_{0.1}S_{10.7}$ glass–ceramic electrolyte samples. A strong peak at 1.7 ppm in ^{7}Li MAS NMR spectra, indicating the Li environment [36]. Therefore, the WS_2 doped strategy for the Li7P3S11 system does not involve the alteration of intrinsic structural units. Figure 3b presents the ^{31}P MAS NMR spectra of $Li_7P_3S_{11}$, $Li_7P_{2.9}W_{0.05}S_{10.85}$, and $Li_7P_{2.8}W_{0.1}S_{10.7}$ glass–ceramic samples. ^{31}P MAS NMR spectrum consists of three obvious peaks with different integral intensities, revealing the sulfur environments around the P atom [37]. These NMR peaks of 106 ppm, 90.8 ppm, and 86 ppm correspond to $P_2S_6^{4-}$, $P_2S_7^{4-}$ and PS_4^{3-} structural units, respectively [38]. The analysis of ^{31}P MAS NMR spectra is in agreement with the analytical findings of Raman spectroscopy. These results suggest that the WS_2 doped strategy for $Li_7P_3S_{11}$-type electrolyte does not generate new structural units (such as POS_3^{3-}).

It is well-known that $Li_7P_3S_{11}$-type glass–ceramic electrolytes are composed of a crystalline and amorphous phase, where the crystalline phase plays an essential role in lithium-ion conduction. The crystalline phase is a high lithium-ion conductor as compared to the amorphous phase. Consequently, the proportion of the conductive crystalline phase determines the ionic conductivity of glass–ceramic electrolytes. The crystalline and amorphous portion ratio is evaluated by the degree of crystallization from the ^{31}P MAS NMR spectrum. As shown in Fig. 3c–e, they display peak deconvolution results of $Li_7P_3S_{11}$, $Li_7P_{2.9}W_{0.05}S_{10.85}$, and $Li_7P_{2.8}W_{0.1}S_{10.7}$ glass–ceramic samples, respectively.

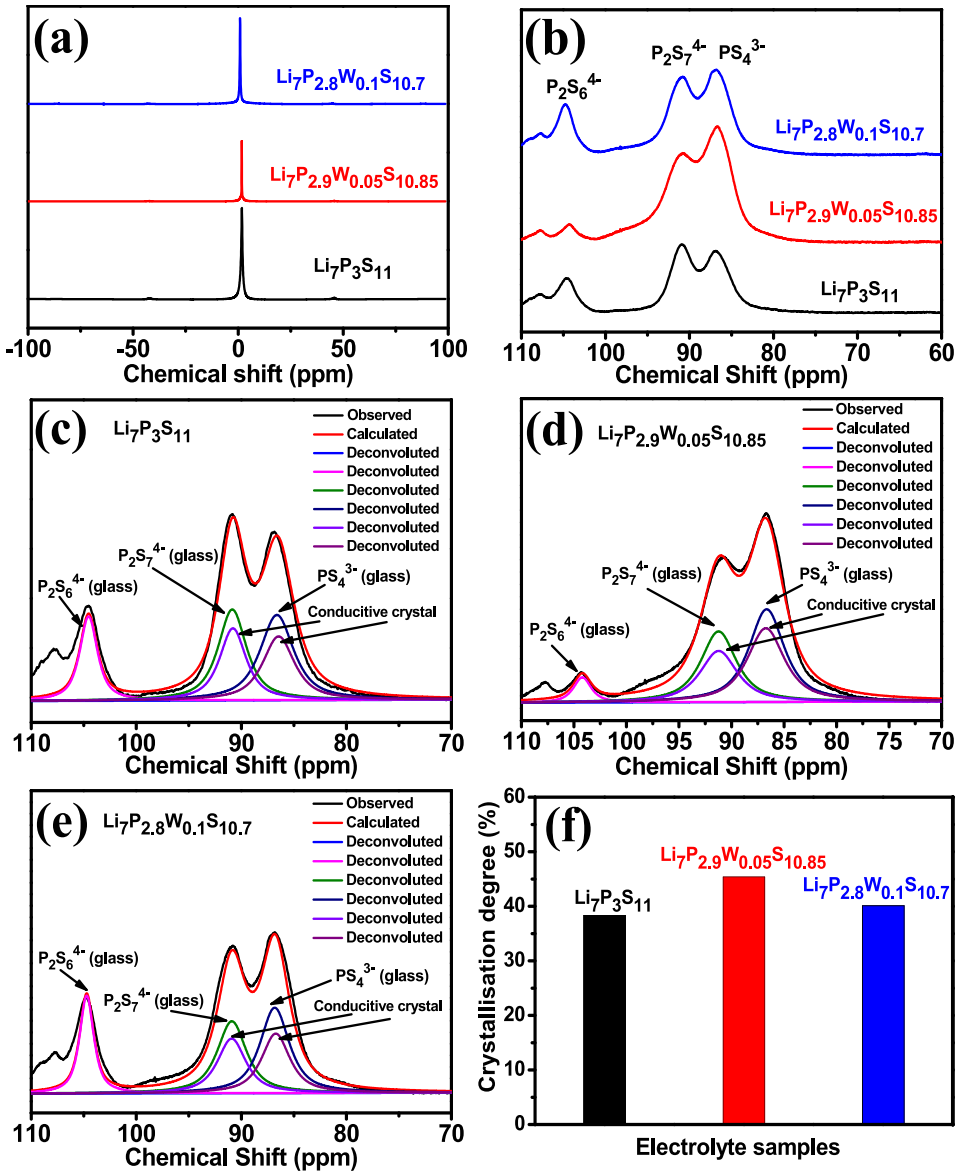

Fig. 3 **a** ^{7}Li MAS NMR spectra of $Li_7P_3S_{11}$, $Li_7P_{2.9}W_{0.05}S_{10.85}$ and $Li_7P_{2.8}W_{0.1}S_{10.7}$ glass–ceramic samples, **b** ^{31}P MAS NMR spectra of $Li_7P_3S_{11}$, $Li_7P_{2.9}W_{0.05}S_{10.85}$ and $Li_7P_{2.8}W_{0.1}S_{10.7}$ glass–ceramic samples, **c**, **d** and **e** peak-deconvolution results of the ^{31}P MAS NMR spectra, **f** the crystallization degree for $Li_7P_3S_{11}$, $Li_7P_{2.9}W_{0.05}S_{10.85}$ and $Li_7P_{2.8}W_{0.1}S_{10.7}$ glass–ceramic samples

The degree of crystallization (X_C) of sulfide electrolytes is calculated according to Eq. (3):

$$X_C = \frac{\Phi_{PS4} + \Phi_{P2S7}}{\Phi_{all}} \times 100 \quad (3)$$

In this equation, the intensity of Φ_{PS4} and Φ_{P2S7} is the crystalline phase, and Φ_{all} is the total intensity of ^{31}P MAS NMR peaks. Consequently, based on Eq. (3), $Li_7P_3S_{11}$, $Li_7P_{2.9}W_{0.05}S_{10.85}$, and $Li_7P_{2.8}W_{0.1}S_{10.7}$ glass–ceramic electrolytes present the degree of crystallization of 38.5%, 45.4%, and 36.2%, as shown in Fig. 3f, respectively. It is evidence that heteroatom doping for Li7P3S11-type glass–ceramic samples would alter the ratio of crystalline and amorphous phases [39, 40]. The newly designed $Li_7P_{2.9}W_{0.05}S_{10.85}$ glass–ceramic electrolyte exhibits the highest value of crystallinity, signifying the highest ionic conductivity as compared to $Li_7P_3S_{11}$ and $Li_7W_{0.1}P_{2.8}S_{10.7}$. In addition, compared to $Li_7P_3S_{11}$ glass–ceramic electrolyte, the amplified lithium transmission channels contribute to the transport of lithium ions, which helps to improve the lithium-ion conductivity of $Li_7P_{2.9}W_{0.05}S_{10.85}$ glass–ceramic electrolyte.

As given in Fig. 4a, the morphology and microstructure of the $Li_7P_{2.9}W_{0.05}S_{10.85}$ glass–ceramic particles are investigated by SEM. It may be seen intuitively that the contact

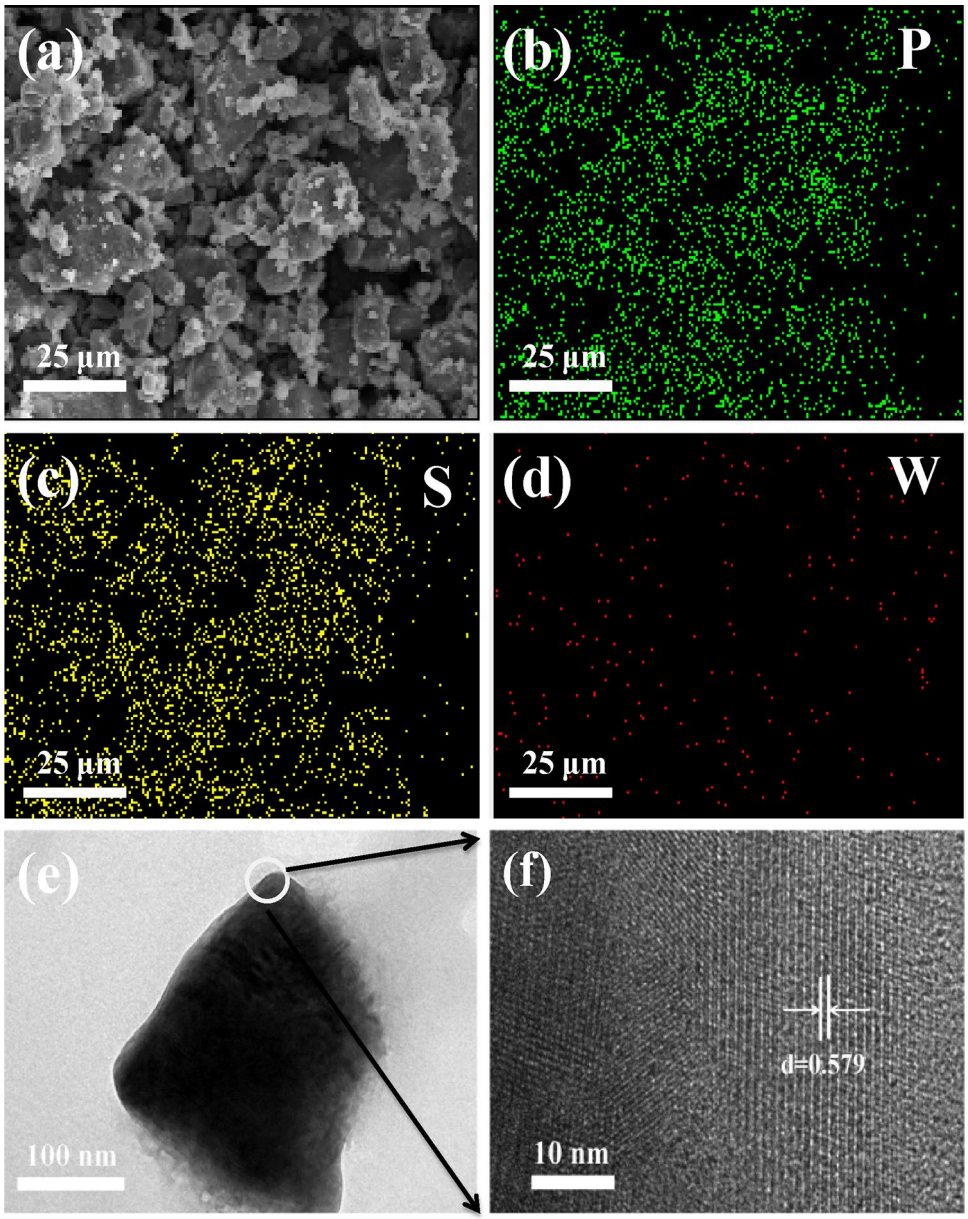

Fig. 4 **a** The SEM of $Li_7P_{2.9}W_{0.05}S_{10.85}$ glass–ceramic electrolyte, **b**, **c**, **d** elemental mapping images of $Li_7P_{2.9}W_{0.05}S_{10.85}$ glass–ceramic electrolyte, **e** the TEM of $Li_7P_{2.9}W_{0.05}S_{10.85}$ glass–ceramic electrolyte, **f** the HRTEM of $Li_7P_{2.9}W_{0.05}S_{10.85}$ glass–ceramic electrolyte

between particles is very close. This phenomenon is mainly due to the heat treatment temperature being above the crystallization temperature. Simultaneously, the EDX mapping results of the $Li_7P_{2.9}W_{0.05}S_{10.85}$ glass–ceramic sample show that P, W, and S elements in Fig. 4b–d are uniformly distributed throughout the sample's surface. It also verifies the uniform doping of WS_2 without any local concentration at one place.

The $Li_7P_3S_{11}$ glass–ceramic electrolyte also delivers the uniform distribution of P and S elements in Figure S4a–c. The high-resolution TEM image is used to investigate the impacts of W-doping on the crystal structure. Figure 4e and f represent the microstructure as well as the crystal structure of the as-prepared $Li_7P_{2.9}W_{0.05}S_{10.85}$ glass–ceramic sample. In Fig. 4e, the microstructure is displayed by an irregular block. Figure 4f, the HRTEM image, demonstrates that the glass–ceramic electrolyte contains both crystalline and amorphous phases, consistent with the SEM observations. The measured lattice distance of the $Li_7P_{2.9}W_{0.05}S_{10.85}$ glass–ceramic sample is 0.579 nm, which corresponds to the lattice distance of the (311) plane [41, 42]. According to the HRTEM result in Figure S5a, b, the lattice distance

of the (311) plane of $Li_7P_3S_{11}$ glass–ceramic electrolyte is 0.576 nm. As a result of the doping of WS_2, the lattice distance is increased.

The as-prepared $Li_7P_{2.9}W_{0.05}S_{10.85}$ solid electrolytes with high ionic conductivity are achieved successfully, which contributes significantly to the outstanding rate performance of the all-solid-state Li-SeS_2 battery. However, the rate capability of the all-solid-state Li-SeS_2 battery is influenced not only by the ionic conductivity of solid-state electrolyte but also depends on the carrier transport path of the composite cathode. Our study aims to improve kinetics by designing a cathode composite enriched with ionic and electronic conducting networks and optimizing transportation factors such as effective conductivity and tortuosity. The tortuosity of the carrier transport path directly determines the ionic and electronic conductivity of composite cathode, which also affects the kinetics feature. The diverse microstructures offer different carrier transport pathways in composite cathodes. By designing the two cathode microstructure architectures, we tailor the tortuosity of the carrier transport path. Common cathode composite (CCC) and interpenetrating network composite cathode (INCC) are designed via extra steps to add conductive agent and softness of as-prepared electrolyte. The detailed concept and preparation process are shown in Figure S6.

The electronic conductivity of the cathode composite can be determined using a sandwich structure. Figure 5a, b exhibits the current–time plot of composite cathodes for the measurement of electronic conductivity. The electronic conductivity (σ_{ele}) of cathode composite is calculated by the formula (4):

$$\sigma_{ele} = \frac{L \cdot I}{S \cdot V} \tag{4}$$

where L is the thickness of the cathode composite, I is the steady-state current, S is the area of the composite cathode, and V is the applied voltage. The electronic conductivity of interpenetrating network composite cathode (INCC) and common cathode composite (CCC) is 1.18 and 0.116 S cm^{-1}. The electronic conductivity of INCC is 10.2 times higher than that of CCC. It is evident that the tailoring interpenetrating network significantly improves the electronic conductivity of cathode composite due to the different dispersion forms of conductive agent. Lithium-ion migration and electrical transport are critical challenges for ideal electrode design.

Furthermore, the ionic conductivities of cathode composites are also explored by a Penta-layer cell via the AC impedance method [43]. The cell consists of a composite cathode, sulfide electrolyte, and lithium foil in Fig. 5c. As

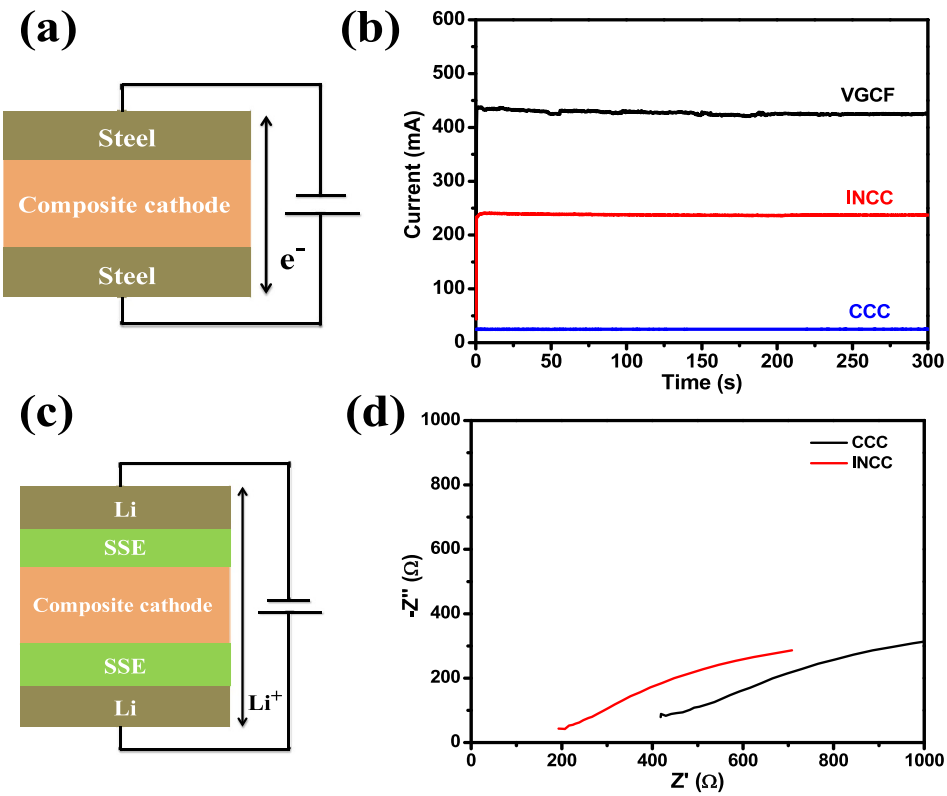

Fig. 5 **a** Sandwich structure of cathode composite, **b** current–time plot of two cathode composites for electronic conductivity measurement, **c** Schematics of a Penta-layer cell upon application of AC impedance, (**b**) AC impedance spectrum of the composite cathodes

shown in Fig. 5d, the resistance of INCC and CCC is 194 and 416 Ω, respectively. According to formula (2), the ionic conductivity of INCC was 1.83×10^{-4} S cm^{-1} and the ionic conductivity of CCC 0.852×10^{-4} S cm^{-1} at room temperature. As a result, the ionic tortuosity factor of INCC and CCC is 6.55 and 14.08 based on the formula (5), respectively. Thus, INCC delivers higher ionic conductivity than CCC. Furthermore, it indicates that ionic transportation in the cathode composite is more significant than the electron transfer. Also, the little fraction of the conductive agent affects the ionic conductivity of composite cathode due to the altered the carrier transport path.

Moreover, Janek et al. explore carrier transport toward optimized cathode composites in all-solid-state batteries [44, 45]. They conclude that complex cathode composite hinders carrier transport and results in tortuous conduction pathways. Therefore, the tortuosity of the electron (or ionic) carrier transport path determines the electron (or ionic) conductivity of the cathode composite. For further quantification and comparison of the electron (or ionic) transport between different systems, the tortuosity factor (t) of the transport path is often considered and calculated by the formula (5):

$$t = \frac{\sigma^{\mathrm{pri}}}{\sigma^{\mathrm{mea}}} \bullet \varphi \tag{5}$$

where σ^{pri} is the electron (or ionic) conductivity of pristine component, σ^{mea} denotes the experimentally measured electron (or ionic) conductivity, and φ is the volume fraction of conductive agent (or sulfide electrolyte). This formula quantifies the effect of a heterogeneous microstructure on the electron transport in the composite cathode. The concept of tortuosity in terms of homogenization enables us to evaluate the hindrance of the charge transport in the complex microstructure. A high tortuosity factor indicates tortuous and hampered transport, corresponding to low electron-transport property [45]. Based on formula (5), the electron tortuosity factor of CCC is 5.49, and the electron tortuosity factor of INCC is 0.54. It indicates that INCC has a significant advantage on electron transport due to the lower tortuosity factor. As a result, interpenetrating network tactics could effectively reduce the tortuosity factor of the electron transport path and lead to rapid transport of electrons in cathode composite. Notably, the reduced tortuosity factor improves the electronic conduction and ion migration resulting in dynamic characteristics of all-solid-state batteries.

As presented in Fig. 6a, reveals the morphology of the CCC. Due to the soft nature of sulfide electrolytes, it is unavoidable to coat the conductive agent within the electrolyte system after ball milling. The ability of carrier transport is significantly reduced. More importantly, the conductive agent is covered inside the electrolyte, and the carrier transport between the electrolytes lacks the necessary channel. Time-of-flight secondary ion mass spectrometry (TOF–SIMS) is employed to study the dispersion of the electrode composite due to ultra-high sensitivity for all

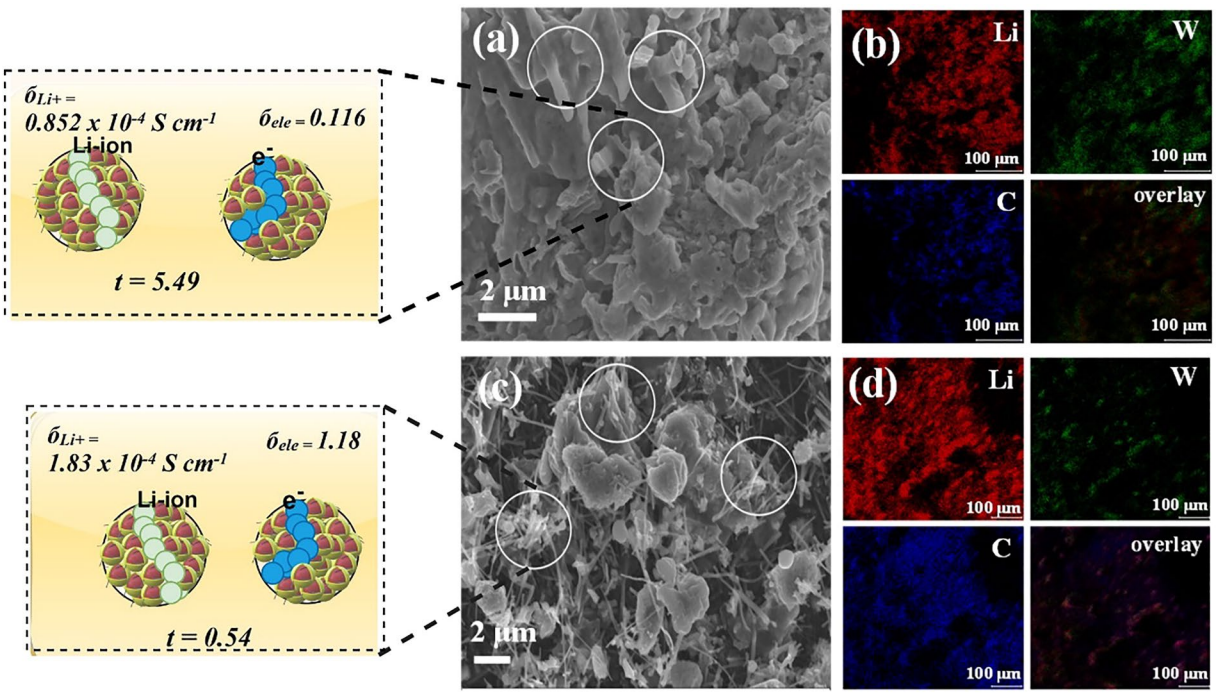

Fig. 6 **a** Morphology of the CCC electrode, **b** TOF–SIMS secondary ion images of CCC electrode, **c** morphology of the INCC electrode, **d** TOF–SIMS secondary ion images of the INCC electrode

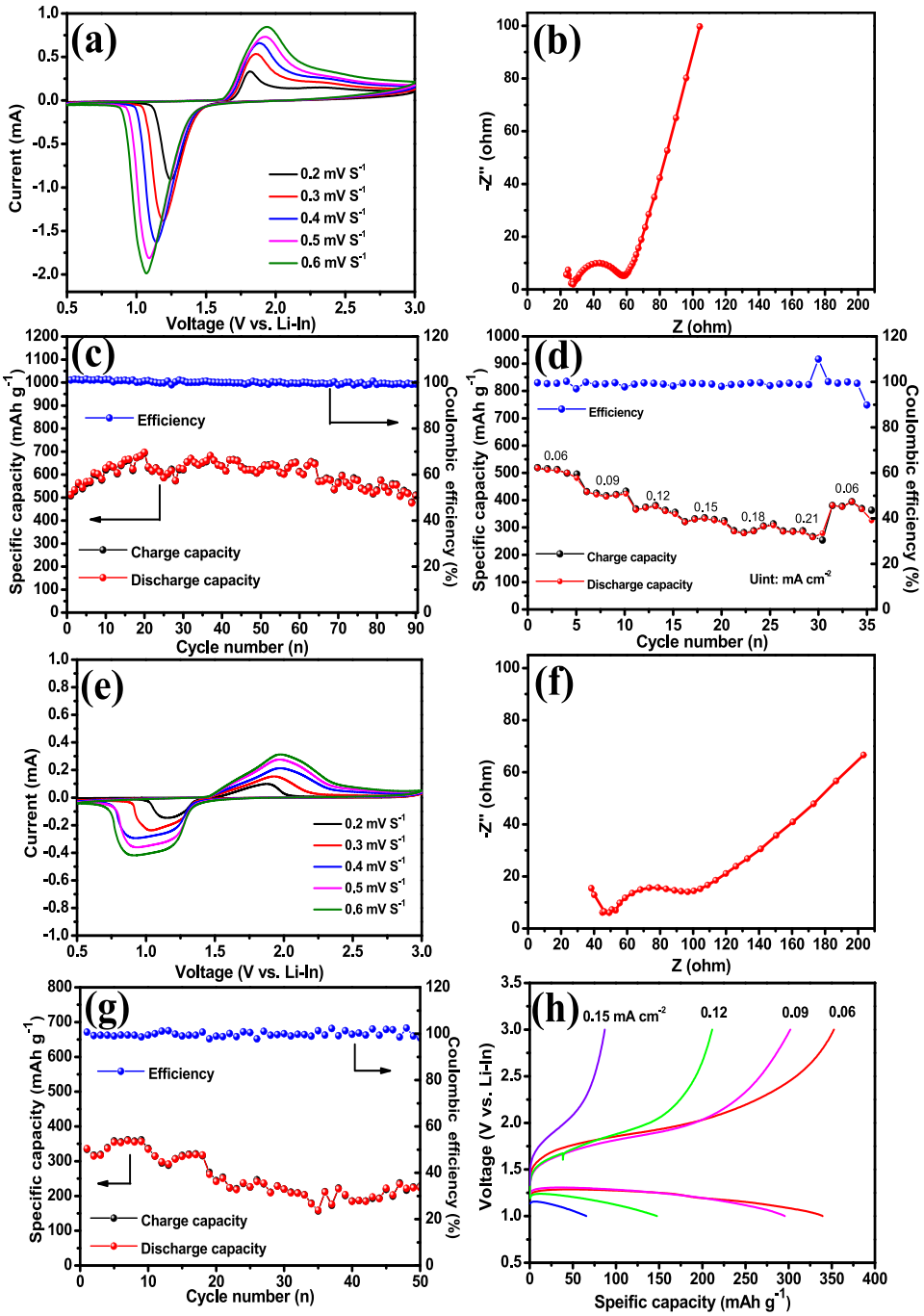

Fig. 7 Electrochemical properties of all-solid-state Li-SeS_2 batteries based on interpenetrating network cathode composite (**a**–**d**) and common cathode composite (**e**–**h**): **a**, **e** cyclic voltammetry curves with different scanning rates in the voltage window of 0.5–3 V; **b**, **f** AC impedance spectra in the frequency range of 1 MHz to 100 Hz; **c**, **g** cycling stability of Li-SeS_2 battery at room temperature; **d**, **h** rate capability of Li-SeS_2 batteries at a different current density at room temperature

chemical elements [46, 47]. Figure 6b displays TOF–SIMS secondary ion images of the CCC and indicates homogeneous dispersion for all the components. Thus, the ball milling method is an excellent choice to obtain a homogeneous composite cathode. In Fig. 6c, we observe some VGCF uncoated with sulfide electrolyte due to lower ball milling speed. These uncovered VGCF conductive agent bridges charge carrier transfer channels among sulfide electrolytes. Thus, we successfully prepare the INCC electrode. As a result, it enhances carrier conductivity in cathode composite and improves rate capability. Moreover, Fig. 6d presents TOF–SIMS secondary ion images of INCC and reveals

better dispersion for all the components, particularly with the lithium image being more intense, indicating their high concentration.

Figure 7 presents the electrochemical properties of all-solid-state Li-SeS_2 batteries based on different cathode composites, where the thickness of solid-state electrolyte is about 0.67 mm. Figure 7a exhibits a series of CV curves for INCC /$Li_7P_{2.9}W_{0.05}S_{10.85}$/Li-In battery at different scan rates ranging from 0.2 to 0.6 mV s^{-1}. In an all-solid-state system, there is only one reduction could be observed at 1.25 V with the scan rate of 0.2 mV s^{-1}, attributed to the formation of Li_2Se/Li_2S instead of long-chain lithium polysulfides/polyselenides [48, 49]. The subsequent anodic scan shows a strong oxidation peak at 1.8 V at 0.2 mV s^{-1}, corresponding to the reversible conversion of SeS_2. Besides, the current peaks of every CV curve gradually increase with the amplifying of scan rate. The all-solid-state Li-SeS_2 batteries display similar redox processes at different sweep rates as well as exhibited superior reversibility at the highest scan rate of 0.6 mV s^{-1}, suggesting the lower polarization of interpenetrating network cathode composite. It evidences that the all-solid-state Li-Se batteries would possess excellent rate capability. On the other hand, compared with CCC/$Li_7P_{2.9}W_{0.05}S_{10.85}$/Li-In battery, the CV curves present unsatisfactory behavior in Fig. 7e. The oxidation/reduction peaks are asymmetrical and gradually become widen as the scanning speed increases. It demonstrates that the greater polarization appears in CCC/$Li_7P_{2.9}W_{0.05}S_{10.85}$/Li-In system.

As shown in Fig. 7b and f, the EIS spectra of all-solid-state Li-SeS_2 batteries have typical characteristics of ionic conductors, with a circular arc in the high-frequency region representing the interface resistance and an inclined line in the low-frequency region exhibiting the ion diffusion. The measured resistance is the point at which the ion-diffusion line intersects the transverse axis. Thus, the resistance of the INCC /$Li_7P_{2.9}W_{0.05}S_{10.85}$/Li-In battery is 60 Ω, and the CCC /$Li_7P_{2.9}W_{0.05}S_{10.85}$/Li-In battery is 100 Ω. Overall, both batteries reveal a relatively small resistance (< 200 Ω). All-solid-state batteries are pressurized under high pressure, which significantly reduces interface and grain boundary resistance. However, under the same condition, INCC/$Li_7P_{2.9}W_{0.05}S_{10.85}$/Li-In battery has a low charge transfer interface resistance of 30 Ω. The value was about half of the CCC /$Li_7P_{2.9}W_{0.05}S_{10.85}$/Li-In battery (about 60 Ω). It proves that a unique interpenetrating network in cathode composite reduces battery impedance and charge transfer impedance simultaneously.

All-solid-state Li-SeS_2 batteries are tested at room temperature in a voltage range of 1–3 V to determine practical capacity, cycling stability, and rate capability. The INCC /$Li_7P_{2.9}W_{0.05}S_{10.85}$/Li-In battery exhibits a high specific capacity of 512 mAh g^{-1} at the first cycle, as shown in Fig. 7c. It also has a high coulombic efficiency of 99% at the current density of 0.06 mA cm^{-1}. The excellent electron transport systems could improve the active material utilization and present much higher capacity and coulombic efficiency. As exhibited in Fig. 7c, the specific capacity of the INCC /$Li_7P_{2.9}W_{0.05}S_{10.85}$/Li-In battery gradually increases as the loop measurement progresses, owing to the activation process of electrode materials. Surprisingly, after the 90th cycle, the INCC /$Li_7P_{2.9}W_{0.05}S_{10.85}$/Li-In battery retains a reversible specific capacity of 506 mAh g^{-1}. Based on the first discharge specific capacity, the capacity retention can reach up to 98.8%. Therefore, INCC /$Li_7P_{2.9}W_{0.05}S_{10.85}$/Li-In battery has an excellent kinetic characteristic. In comparison, the CCC /$Li_7P_{2.9}W_{0.05}S_{10.85}$/Li-In battery only delivers a relatively low capacity of 336 mAh g^{-1} with a current density of 0.06 mA cm^{-1} at the first cycle presented in Fig. 7g. It only offers a relatively low capacity of 223 mAh g^{-1} after 50 cycles with capacity retention of 66.4% cycles due to poor electronic conductivity. As a result, it has a significant impact on active material utilization and electrochemical reaction kinetics.

Figure 7d depicts the rate capability of INCC/$Li_7P_{2.9}W_{0.05}S_{10.85}$/Li-In battery. In detail, the all-solid-state battery presents discharge capacities of 515, 430, 364, 329, 307 and 285 mAh g^{-1} at various current density of 0.06, 0.09, 0.12, 0.15, 0.18 and 0.21 mA cm^{-1}, respectively. While recovering current density to 0.06 mA cm^{-1}, the capacity is partially restored. This result suggests that INCC/$Li_7P_{2.9}W_{0.05}S_{10.85}$/Li-In battery has superior rate performance due to superior electrochemical kinetic characteristics. In contrast, the rate capability of the CCC/$Li_7P_{2.9}W_{0.05}S_{10.85}$/Li-In battery could not be performed in the manner described above due to poor cycling stability. Only one measurement is performed at each current density to obtain intrinsic rate capability. As presented in the Fig. 6h, CCC/$Li_7P_{2.9}W_{0.05}S_{10.85}$/Li-In battery displays lower capacities of 339, 295, 174 and 65 mAh g^{-1} at different current density of 0.06, 0.09, 0.12 and 0.15 mA cm^{-1}, respectively. It indicates that the reaction kinetic of CCC/$Li_7P_{2.9}W_{0.05}S_{10.85}$/Li-In is inadequate.

In comparison, all-solid-state Li-Se batteries with an interpenetrating electron network cathode have a higher specific capacity, better cycling stability, and superior rate capability. Thus, the interpenetrating network could prevent ineffective contact with no effective conducting agent, avoiding significant capability degradation. Due to weak electronic/ionic conductivity and low active material usage, the common cathode composite (CCC) exhibits low capacity, poor cycling stability, and rate capability.

It is well known that the diffusion coefficient (D_{Li+}) is one of the essential factors that evaluate the kinetics of the electrochemical energy storage devices [50–52]. The galvanostatic intermittent titration technique (GITT) is utilized to explore the diffusion coefficient of all-solid-state Li-Se

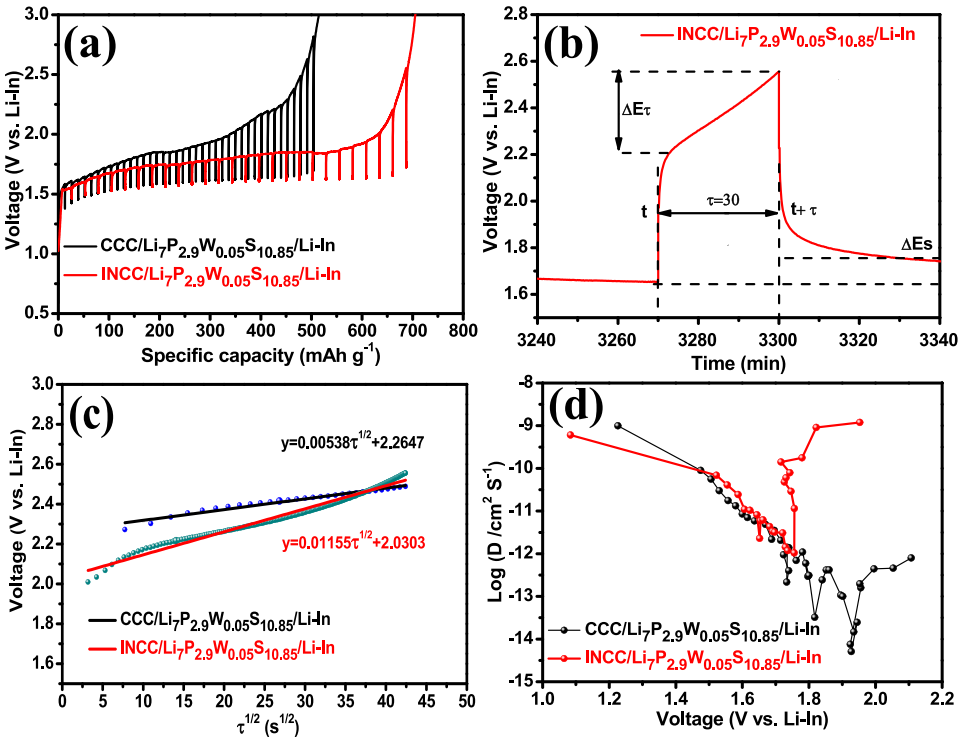

Fig. 8 **a** GITT curves of CCC/$Li_7P_{2.9}W_{0.05}S_{10.85}$/Li-In and INCC/$Li_7P_{2.9}W_{0.05}S_{10.85}$/Li-In system at the process of charge, **b** the potential profile before, during, and after a constant current pulse with schematic labeling, **c** the corresponding linear behavior of E against $\tau^{1/2}$, **d** the calculated Li^+ diffusion coefficients at the process of charge

battery. The diffusion coefficient (D_{Li^+}) can be calculated according to equation (6):

$$D_{Li^+} = \frac{4}{\pi\tau}\left(\frac{mV_m}{MA}\right)^2\left(\frac{\Delta E_s}{\Delta E_\tau}\right)^2 \quad (6)$$

where m and M are mass and molar mass of the SeS_2 (g, g mol^{-1}), respectively. Vm represents the molar volume of SeS_2. A is contact area (cm^2). τ is pulse duration (s). ΔEs and $\Delta E\tau$ can be obtained from the single potential profile before, during, and after a constant current pulse. Figure 8a reveals the GITT curves of CCC /$Li_7P_{2.9}W_{0.05}S_{10.85}$/Li-In and INCC/$Li_7P_{2.9}W_{0.05}S_{10.85}$/Li-In battery systems. The all-solid-state Li-Se battery only exhibits one plateau during the charging process between 1.0 and 3.0 V. Evidently, the SeS_2 electrode in an all-solid-state battery presents a one-step solid–solid phase transition between Li_2Se and SeS_2, which coincides with CV results of the Se cathode. In addition, Fig. 8b and Figure S11 reveal the single potential profile before, during, and after a constant current pulse, contributing to acquiring ΔEs and $\Delta E\tau$ at a constant current pulse. As given in Fig. 8c, it exhibits a straight line behavior between the responsible potential and time period $\tau^{1/2}$. Thus, the diffusion coefficients for both composite cathodes can be calculated according to the simplified Eq. (6). Figure 8d delivers the calculated D_{Li+} for composite cathodes from the GITT profiles during the charging process. Overall, D_{Li+} values for two cathodes show a similar variation trend during charging (from 1 to 3 V) with the different order, where the D_{Li+} values decrease first and then increase. The minimum D_{Li+} values for INCC/$Li_7P_{2.9}W_{0.05}S_{10.85}$/Li-In battery are observed at around 1.75 V in Fig. 8c, ascribing to the voltage plateaus during the charging process. It can be seen that the D_{Li+} value ranges from 10^{-9} to 10^{-12} cm^2 s^{-1} during the charging process. By comparison, the CCC/$Li_7P_{2.9}W_{0.05}S_{10.85}$/Li-In battery presents less D_{Li+} value range from 10^{-9} to 10^{-14} cm^2 s^{-1} during the charging process. Thus, the diffusion coefficient of INCC/$Li_7P_{2.9}W_{0.05}S_{10.85}$/Li-In battery is higher on average than that of CCC/$Li_7P_{2.9}W_{0.05}S_{10.85}$/Li-In battery. One of the most important reasons that ionic/electronic diffusion path is shortened with the help of an interpenetrating network, generating superior kinetic property. Moreover, the $Li_7P_{2.9}W_{0.05}S_{10.85}$ sulfide electrolyte with high ionic conductivity also improves the kinetic property of all-solid-state batteries. Thus, the enhancing rate capability of an all-solid-state battery mainly depends on the design of an excellent composite cathode and the development of high ionic conductivity electrolytes.

Conclusion

In conclusion, the $Li_7P_{2.9}W_{0.05}S_{10.85}$ sulfide electrolyte is prepared by W doping, which delivers a high ionic conductivity of 2.0 mS cm^{-1} at room temperature. In addition, the cathode composite with an interpenetrating network is also tailored by three-step ball grinding, whose electronic conductivity and ionic conductivity are 1.18 S cm^{-1} and 0.183 mS cm^{-1}, respectively. The electronic conductivity of ICCC is 10.2 times, and the ionic conductivity of INCC is 2.1 times that of CCC. The reason is that interpenetrating network tactics could effectively reduce the tortuosity factor of the carrier transport path, leading to the rapid transport of electrons and ions in the composite cathode. The cathode composite with an interpenetrating network is applied to all-solid-state Li-SeS_2 batteries, which shows a high specific capacity of 512 mAh g^{-1} at the current density of 0.06 mA cm^{-1}. Significantly, it also reveals excellent rate capability due to enhanced electrochemical dynamics. This work provides a feasible way to tailor the high ionic conductivity electrolyte and interpenetrating ion/electron network composite for high rate all-solid-state Li-SeS_2 batteries.

Experimental Section

Preparation of Sulfide Solid-State Electrolytes

$70Li_2S$-(30-x)P_2S_5-xWS_2 (x = 0, 1, 2) sulfide glass–ceramic electrolytes were prepared using a high-energy ball milling method and appropriate heat treatment. Li_2S (Alfa Aesar, 99.9%), P_2S_5 (Macklin, 99%), and WS_2 (Aladdin, 99.9%) were used as precursors without further treatment. Firstly, appropriate precursors with an exact molar ratio were weighed in the argon glove box ($O_2 < 0.1$ ppm, $H_2O < 0.1$ ppm) due to the reaction with oxygen and moisture in the air. The above precursors were placed into a zirconia pot filled with zirconia balls and then ground by the high-energy ball-milling machine (Fritsch, Germany). After high energy ball milling (45 h, 510 rpm), the obtained glass sample was heated at a suitable temperature. Finally, $Li_7P_3S_{11}$ ($70Li_2S$-$30P_2S_5$), $Li_7P_{2.9}W_{0.05}S_{10.85}$ ($70Li_2S$-$29P_2S_5$-$1WS_2$), and $Li_7P_{2.8}W_{0.1}S_{10.7}$ ($70Li_2S$-$28P_2S_5$-$2WS_2$) glass–ceramic electrolyte were obtained successfully.

Preparation of SeS_2/CNT composite

Commercial carbon nanotubes (CNT) power (purity > 95%, diameter 10–20 nm, length 10–30) was purchased from Nanjing XFNANO technology Co., Ltd. The CNT power was treated with concentrated hydrochloric acid stirring for 10 h to wash away any metal ions, suction-washed, and then dried at 90 °C in an oven. The commercial SeS_2 power was purchased from (Alfa Aesar, 99.9%). SeS_2/CNT composite was prepared as to the reported melt-diffusion method. Typically, SeS_2 and CNT power with the weight ratio of 7:3 were mixed uniformly by grinding. Then they were heated at 155 °C for 12 h with a heating rate of 5 °C min^{-1} in a sealed vessel. After cooling to room temperature, the SeS_2/CNT composite was prepared successfully. Figure S5 displays the morphology feature SeS_2/CNT composite, indicating better dispersion for SeS_2 and CNT. The XRD patterns of pristine SeS_2 and SeS_2/CNT samples are exhibited in Figure S6. It demonstrates that the melt-diffusion method does not generate new materials and change the crystal structure of SeS_2.

Preparation of Cathode Composites

Vapor-grown carbon fiber (VGCF) power was purchased from Japan Showa Denko. Before using as a conductive agent in all-solid-state batteries, VGCF was heat-treated at 80 °C for 12 h to remove the moisture. A grinding pattern of two steps prepared the CCC electrode. SeS_2/CNT and VGCF were ground with a weight ratio of 3: 1: at a rotating speed of 360 rpm. Then, the above mixture and sulfide electrolyte were smoothed with a weight ratio of 4: 6 at the same rate.

The interpenetrating network composite cathode (INCC) was designed by a ball milling pattern of three steps. In detail, a mixture of SeS_2/CNT and VGCF with a weight ratio of 3:0.5 was grinded by a rotating speed of 360 rpm. Following, the above mixture and sulfide electrolyte with a weight ratio of 3.5: 6 was milled at the same speed. Last, the above mixture and VGCF with a weight ratio of 3.5: 6 was milled at a rotating speed of 100 rpm. In addition, all the above processes were performed in an argon atmosphere.

Electronic Conductivity Test of Cathode Composites

Cathode Composite (100 mg) or VGCF (100 mg) was placed into a mould and pressed into a sandwich structure with stainless steel under huge pressure (about 240 MPa). The electrochemical workstation was used to perform potentiostatic measurement at a bias voltage of 5 mV, and the current changes were recorded.

Ion Conductivity Test of Cathode Composites

Cathode Composite (100 mg) was placed into a mould and pressed into a table under a pressure of 240 MPa. Then, sulfide electrolyte powder (100 mg) was added to one side of the composite cathode table and pressed into the table. Next, sulfide electrolyte powder (100 mg) was again added to another side of the composite cathode table and pressed into a table under about 240 MPa pressure. Last, Li/sulfide

electrolyte/composite cathode/sulfide electrolyte/Li battery was assembled by placing lithium sheets on both sides of the composite layer. The electrochemical workstation was employed to record the voltage response of a Penta-layer cell to a charging current of 0.1 mA.

Structure and Morphology Characterization

X-ray diffraction (XRD) measurements were performed on the Bruker D8 Advance using Cu-Kα radiation with a scanning step of 5° min^{-1}**.** Solid-state nuclear magnetic resonance (NMR) spectra were conducted on Bruker Ascend 700 M spectrometer to explore ^{31}P and ^{7}Li. Scanning electron microscope (SEM) and elemental mapping were used using S-4800 field-emission scanning electron microscopy (Hitachi, Japan). Transmission electron microscopy (TEM) and high-resolution transmission electron microscope (HRTEM) were measured on an S-4800 transmission electron microscope (Hitachi, Japan) operated at 400 kV. X-ray photoelectron spectroscopy (XPS) measurements were performed with the Thermo Fischer (ESCALAB 250Xi) instrument using Al Kα radiation source. The differential thermal analysis (DTA) of the sulfide glass sample was determined at a temperature range from 30 to 300 °C (Hitachi, TG–DTA 6200) with a heating rate of 10 °C min^{-1} under Ar atmosphere. Raman spectra were measured at an excitation laser beam wavelength of 532 nm using a Renishaw in Via Raman microscope. The TOF–SIMS measurements were performed on an ION-TOF (GmbH, Germany) TOF–SIMS IV with a bismuth liquid metal ion source.

Fabrication of All-Solid-State Battery

All-solid-state Li-Se batteries were fabricated by powder compression pattern in glove box ($O_2 < 0.1$ ppm, $H_2O < 0.1$ ppm). These batteries have consisted of as-prepared $Li_7P_{2.9}W_{0.05}S_{10.85}$ glass–ceramic electrolyte, SeS_2/CNT composite cathode, and Li-In alloy anode. The detailed steps were as follows. Initially, solid-state electrolyte (150 mg) was assembled firstly in the mold under great pressure. Then, the cold pressing method was employed to construct SeS_2/CNT cathode composite. Finally, Li-In alloy (10 wt.% Li) was pressed on the bottom of the interlayer electrolyte.

Electrochemical Characterization

A blocking electrode system was employed to explore the lithium ionic conductivity of sulfide glass–ceramic electrolytes. The electrochemical impedance spectroscopy (EIS) of the blocking electrode system, including sulfide glass–ceramic electrolyte, was performed by the electrochemical workstation (PARSTAT 2273, USA) with an amplitude of 15 mV at frequencies ranging from 1 MHz to 100 Hz. The non-blocking system tested the electrochemical window of glass–ceramic electrolyte. The cyclic voltammetry (CV) curve of the non-blocking electrode system was characterized at the voltage from − 0.5 to 5 V with a scan rate of 1 mV s^{-1}.

The electrochemical workstation measured the cyclic voltammetry and Nyquist plots of assembled all-solid-state Li-Se batteries. Specifically, the CV curves were recorded with the voltage range from 0 to 3.5 V (vs Li-In) at different scan rates. The Nyquist plots were performed at frequencies ranging from 1 MHz to 100 Hz by applying an alternating current voltage of 15 mV amplitude. The galvanostatic charge/discharge behavior and rate capability of assembled cells were examined by using an advanced battery test system (LAND, China) at room temperature. The specific capacity of the assembled cell was calculated according to the weight of SeS_2 in the composite cathode. All electrochemical measurements were performed in an argon-filled atmosphere. Galvanostatic intermittent titration technique (GITT) experiments were conducted at the Land battery testing system. The two cells were charged at a constant current of 0.015 mA cm^{-1} with an interval of 30 min followed by an open-circuit stand for 120 min to allow the cell potential to relax to its steady-state values. The procedure was repeated for the full electrochemical window.

Supplementary Information The online version contains supplementary material available at https://doi.org/10.1007/s42765-021-00123-6.

Acknowledgements This work is supported by the National Natural Science Foundation of China (No. 21975025, 21203008, 51772030), the National Key Research and Development Program of China "New Energy Project for Electric Vehicle" (No. 2016YFB0100204), and the Nature Science Foundation of Beijing Municipality (No. 2172051). State Key Laboratory also funds the project for Modification of Chemical Fibers and Polymer Materials, Donghua University. DTA, XRD, XPS, and NMR measurements were performed in the Analysis & Testing Center, Beijing Institute of Technology.

Declarations

Conflict of interest The authors state that there are no conflicts of interest to disclose.

References

1. Yang CP, Xin S, Yin YX, Ye H, Zhang J, Guo YG. An advanced selenium-carbon cathode for rechargeable lithium-selenium batteries. *Angew Chem Int Ed* **2013**;*52*:8363.

2. Armand M, Tarascon J-M. Building better batteries. *Nature* **2008**;*451*:652.
3. Li X, Liang J, Li X, Wang C, Luo J, Li R, Sun X. High-performance all-solid-state Li-Se batteries induced by sulfide electrolytes. *Energy Environ Sci* **2018**;*11*:2828.
4. Cai W, Yao Y-X, Zhu G-L, Yan C, Jiang L-L, He C, Huang J-Q, Zhang Q. A review on energy chemistry of fast-charging anodes. *Chem Soc Rev* **2020**;*49*:3806.
5. Eftekhari A. The rise of lithium-selenium batteries. *Sustain Energy Fuels* **2017**;*1*:14.
6. Zeng L-C, Li W-H, Jiang Y, Yu Y. Recent progress in Li-S and Li-Se batteries. *Rare Met* **2017**;*36*:339.
7. Abouimrane A, Dambournet D, Chapman KW, Chupas PJ, Weng W, Amine K. A new class of lithium and sodium rechargeable batteries based on selenium and selenium-sulfur as a positive electrode. *J Am Chem Soc* **2012**;*134*:4505.
8. Lee JT, Kim H, Oschatz M, Lee DC, Wu F, Lin HT, Zdyrko B, Cho WI, Kaskel S, Yushin G. Micro-and mesoporous carbide-derived carbon-selenium cathodes for high-performance lithium selenium batteries. *Adv Energy Mater* **2015**;*5*:1400981.
9. Wang WP, Zhang J, Yin YX, Duan H, Chou J, Li SY, Yan M, Xin S, Guo YG. A rational reconfiguration of electrolyte for high-energy and long-life lithium-chalcogen batteries. *Adv Mater* **2020**;*32*:2000302.
10. Liu F, Wang L, Zhang Z, Shi P, Feng Y, Yao Y, Ye S, Wang H, Wu X, Yu Y. A mixed lithium-ion conductive Li_2S/Li_2Se protection layer for stable lithium metal anode. *Adv Func Mater* **2020**;*30*:2001607.
11. Yi Z, Yuan L, Sun D, Li Z, Wu C, Yang W, Wen Y, Shan B, Huang Y. High-performance lithium-selenium batteries promoted by heteroatom-doped microporous carbon. *J Mater Chem A* **2015**;*3*:3059.
12. Yang X, Luo J, Sun X. Towards high-performance solid-state Li-S batteries: from fundamental understanding to engineering design. *Chem Soc Rev* **2020**;*49*:2140.
13. Chen S, Xie D, Liu G, Mwizerwa JP, Zhang Q, Zhao Y, Xu X, Yao X. Sulfide solid electrolytes for all-solid-state lithium batteries: structure, conductivity, stability and application. *Energy Storage Mater* **2018**;*14*:58.
14. Zheng F, Kotobuki M, Song S, Lai M, Lu L. Review on solid electrolytes for all-solid-state lithium-ion batteries. *J Power Sources* **2018**;*389*:198.
15. Sun C, Liu J, Gong Y, Wilkinson DP, Zhang J. Recent advances in all-solid-state rechargeable lithium batteries. *Nano Energy* **2017**;*33*:363.
16. Manthiram A, Yu X, Wang S. Lithium battery chemistries enabled by solid-state electrolytes. *Nat Rev Mater* **2017**;*2*:1.
17. Ren H-T, Zhang Z-Q, Zhang J-Z, Peng L-F, He Z-Y, Yu M, Yu C, Zhang L, Xie J, Cheng S-J. Improvement of stability and solid-state battery performances of annealed $70Li_2S$-$30P_2S_5$ electrolytes by additives. *Rare Met* **2022**;41:106.
18. Wu J, Liu S, Han F, Yao X, Wang C. Lithium/sulfide all-solid-state batteries using sulfide electrolytes. *Adv Mater* **2021**;*33*:2000751.
19. Deng Z, Zhang Z, Lai Y, Liu J, Liu Y, Li J. A sulfur-carbon composite for lithium/sulfur battery based on activated vapor-grown carbon fiber. *Solid State Ionics* **2013**;*238*:44.
20. Yoon K, Kim J-J, Seong WM, Lee MH, Kang K. Investigation on the interface between $Li_{10}GeP_2S_{12}$ electrolyte and carbon conductive agents in all-solid-state lithium battery. *Sci Rep* **2018**;*8*:1.
21. Zheng H, Yang R, Liu G, Song X, Battaglia VS. Cooperation between active material, polymeric binder and conductive carbon additive in lithium ion battery cathode. *J Phys Chem C* **2012**;*116*:4875.
22. Sun D, Tan Z, Tian X, Ke F, Wu Y, Zhang J. Graphene: A promising candidate for charge regulation in high-performance lithium-ion batteries. *Nano Res* **2021**;*14*:1.
23. Zhang W, Leichtweiß T, Culver SP, Koerver R, Das D, Weber DA, Zeier WG, Janek J. The detrimental effects of carbon additives in $Li_{10}GeP_2S_{12}$-based solid-state batteries. *ACS Appl Mater Interfaces* **2017**;*9*:35888.
24. Hu Y, Zhong Y, Qi L, Wang H. Inorganic/polymer hybrid layer stabilizing anode/electrolyte interfaces in solid-state Li metal batteries. *Nano Res* **2020**;*13*:3230.
25. Deng S, Sun Y, Li X, Ren Z, Liang J, Doyle-Davis K, Liang J, Li W, Norouzi Banis M, Sun Q. Eliminating the detrimental effects of conductive agents in sulfide-based solid-state batteries. *ACS Energy Lett* **2020**;*5*:1243.
26. Xu R, Xia X, Li S, Zhang S, Wang X, Tu J. All-solid-state lithium–sulfur batteries based on a newly designed $Li_7P_{2.9}Mn_{0.1}S_{10.7}I_{0.3}$ superionic conductor. *J Mater Chem A* **2017**;*5*:6310.
27. Zhang Y, Chen R, Liu T, Shen Y, Lin Y, Nan C-W. High capacity, superior cyclic performances in all-solid-state lithium-ion batteries based on $78Li_2S$-$22P_2S_5$ glass-ceramic electrolytes prepared via simple heat treatment. *ACS Appl Mater Interfaces* **2017**;*9*:28542.
28. Busche MR, Weber DA, Schneider Y, Dietrich C, Wenzel S, Leichtweiss T, Schröder D, Zhang W, Weigand H, Walter D. In situ monitoring of fast Li-ion conductor $Li_7P_3S_{11}$ crystallization inside a hot-press setup. *Chem Mater* **2016**;*28*:6152.
29. Park M, Jung H-G, Jung WD, Cho SY, Yun B-N, Lee YS, Choi S, Ahn J, Lim J, Sung JY. Chemically evolved composite lithium-ion conductors with lithium thiophosphates and nickel sulfides. *ACS Energy Lett* **2017**;*2*:1740.
30. Wenzel S, Weber DA, Leichtweiss T, Busche MR, Sann J, Janek J. Interphase formation and degradation of charge transfer kinetics between a lithium metal anode and highly crystalline $Li_7P_3S_{11}$ solid electrolyte. *Solid State Ionics* **2016**;*286*:24.
31. Altavilla C, Sarno M, Ciambelli P. A novel wet chemistry approach for the synthesis of hybrid 2D free-floating single or multilayer nanosheets of MS_2@ oleylamine (M=Mo, W). *Chem Mater* **2011**;*23*:3879.
32. Rajagopal R, Ryu K-S. Evaluation of $Li_6P_2S_8I$ solid electrolyte for all solid-state lithium battery applications. *Chem Eng J* **2020**;*402*:126179.
33. Wang Z, Jiang Y, Wu J, Jiang Y, Huang S, Zhao B, Chen Z, Zhang J. Reaction mechanism of Li_2S-P_2S_5 system in acetonitrile based on wet chemical synthesis of $Li_7P_3S_{11}$ solid electrolyte. *Chem Eng J* **2020**;*393*:124706.
34. Wu Z, Xie Z, Yoshida A, An X, Wang Z, Hao X, Abudula A, Guan G. Novel SeS_2 doped Li_2S-P_2S_5 solid electrolyte with high ionic conductivity for all-solid-state lithium sulfur batteries. *Chem Eng J* **2020**;*380*:122419.
35. Ge Q, Zhou L, Lian Y-m, Zhang X, Chen R, Yang W. Metal-phosphide-doped $Li_7P_3S_{11}$ glass-ceramic electrolyte with high ionic conductivity for all-solid-state lithium-sulfur batteries. *Electrochem Commun* **2018**;*97*:100.
36. Kaus M, Stöffler H, Yavuz M, Zinkevich T, Knapp M, Ehrenberg H, Indris S. Local structures and Li ion dynamics in a $Li_{10}SnP_2S_{12}$-based composite observed by multinuclear solid-state nmr spectroscopy. *J Phys Chem C* **2017**;*121*:23370.
37. Hirai K, Tatsumisago M, Takahashi M, Minami T. ^{29}Si and ^{31}P MAS-NMR spectra of Li_2S-SiS_2-Li_3PO_4 rapidly quenched glasses. *J Am Ceram Soc* **1996**;*79*:349.
38. Ahmad N, Zhou L, Faheem M, Tufail MK, Yang L, Chen R, Zhou Y, Yang W. Enhanced air stability and high Li-Ion conductivity of $Li_{6.988}P_{2.994}Nb_{0.2}S_{10.934}O_{0.6}$ glass-ceramic electrolyte for all-solid-state lithium-sulfur batteries. *ACS Appl Mater Interfaces* **2020**;*12*:21548.
39. Zhou L, Tufail MK, Yang L, Ahmad N, Chen R, Yang W. Cathode-doped sulfide electrolyte strategy for boosting all-solid-state lithium batteries. *Chem Eng J* **2020**;*391*:123529.
40. Tufail MK, Zhou L, Ahmad N, Chen R, Faheem M, Yang L, Yang W. A novel air-stable $Li_7Sb_{0.05}P_{2.95}S_{10.5}I_{0.5}$ superionic conductor

glass-ceramics electrolyte for all-solid-state lithium-sulfur batteries. *Chem Eng J* **2021**;*407*:127149.
41. Eckert H, Zhang Z, Kennedy JH. Structural transformation of non-oxide chalcogenide glasses. The short-range order of lithium sulfide (Li2S)-phosphorus pentasulfide (P2S5) glasses studied by quantitative phosphorus-31, lithium-6, and lithium-7 high-resolution solid-state NMR. *Chem Mater* **1990**;*2*:273.
42. Seino Y, Nakagawa M, Senga M, Higuchi H, Takada K, Sasaki T. Analysis of the structure and degree of crystallisation of $70Li_2S$-$30P_2S_5$ glass ceramic. *J Mater Chem A* **2015**;*3*:2756.
43. Kaiser N, Spannenberger S, Schmitt M, Cronau M, Kato Y, Roling B. Ion transport limitations in all-solid-state lithium battery electrodes containing a sulfide-based electrolyte. *J Power Sources* **2018**;*396*:175.
44. Bielefeld A, Weber DA, Janek Jr. Modeling effective ionic conductivity and binder influence in composite cathodes for all-solid-state batteries. *ACS Applied Mater Interfaces* **2020**;*12*:12821.
45. Dewald GF, Ohno S, Hering JG, Janek J, Zeier WG. Analysis of charge carrier transport toward optimized cathode composites for all-solid-state Li-S batteries. *Batteries Supercaps* **2021**;*4*:183.
46. Song W, Scholtis ES, Sherrell PC, Tsang DK, Ngiam J, Lischner J, Fearn S, Bemmer V, Mattevi C, Klein N. Electronic structure influences on the formation of the solid electrolyte interphase. *Energy Environ Sci* **2020**;*13*:4977.
47. Ryu J, Kang J, Kim H, Lee JH, Lee H, Park S. Electrolyte-mediated nanograin intermetallic formation enables superionic conduction and electrode stability in rechargeable batteries. *Energy Storage Materials* **2020**;*33*:164.
48. Li Z, Zhang J, Wu HB, Lou XW. An improved Li-SeS_2 battery with high energy density and long cycle life. *Adv Energy Mater* **2017**;*7*:1700281.
49. Cui Y, Abouimrane A, Lu J, Bolin T, Ren Y, Weng W, Sun C, Maroni VA, Heald SM, Amine K. (De) Lithiation mechanism of Li/SeS_x (x=0–7) batteries determined by in situ synchrotron X-ray diffraction and X-ray absorption spectroscopy. *J Am Chem Soc* **2013**;*135*:8047.
50. Jiang M, Liu G, Zhang Q, Zhou D, Yao X. Ultrasmall Li_2S-carbon nanotube nanocomposites for high-rate all-solid-state lithium-sulfur batteries. *ACS Appl Mater Interfaces* **2021**;*13*:18666.
51. Li P, Zheng X, Yu H, Zhao G, Shu J, Xu X, Sun W, Dou SX. Electrochemical potassium/lithium-ion intercalation into $TiSe_2$: kinetics and mechanism. *Energy Storage Mater* **2019**;*16*:512.
52. Srout M, Kwon NH, Ben Youcef H, Semlal N, Fromm KM, Saadoune I. $Li_{0.5}Ni_{0.5}Ti_{1.5}Fe_{0.5}(PO_4)_3$/C electrode material for lithium ion batteries exhibiting faster kinetics and enhanced stability. *ACS Appl Mater Interfaces* **2020**;*12*:18496.

Lei Zhou received his master degree from Nanjing Tech University in 2017. Currently, he is a Ph.D. candidate at the Beijing Institute of Technology. His research interests focus on the development and application of sulfide solid-state electrolytes for all-solid-state lithium batteries.

Muhammad Khurram Tufail is a Post-doctoral fellow at Qingdao University. He was received his master degree from HEJ Research Institute of Chemistry, ICCBS, Pakistan, and Ph.D. from Beijing Institute of Technology, China. His research interests focus on the development and application of sulfide-based solid electrolytes for all-solid-state lithium batteries.

Yaozu Liao received his Ph.D degree in 2011 from Tongji University (with Prof. Xin-Gui Li), during which he also worked as a visiting scholar at the University of California, Los Angeles (with Prof. Richard Kaner). Then after worked as a lecturer at the University of Shanghai for Science and Technology, he continued his Marie Curie and Alexander von Humboldt post-doc research at the University of Bristol, UK, and Technical University of Berlin, Germany. In 2015, Yaozu Liao joined State Key Laboratory for Modification of Chemical Fibers and Polymer Materials and Donghua University as a full professor. His research focuses on functional fibers and porous polymers.

Niaz Ahmad received his Ph.D. degree from the school of chemistry and chemical engineering, Beijing Institute of Technology, China, in 2021. His research interests focus on the sulfide solid-state electrolytes for high-performance all-solid-state lithium batteries.

Peiwen Yu received her master degree at Beijing institute of technology in 2018. Currently, she is a Ph.D. candidate majoring in the school of chemistry and chemical engineering, Beijing institute of technology. Her research focuses on the design and application of sulfide solid-state electrolytes for high-performance all-solid-state lithium batteries.

Tinglu Song is an assistant professor and a senior engineer at the Experimental Centre of Advanced Materials (ECAM), Beijing Institute of Technology. His research focuses on polymer materials, flame retardant materials and aerosol catalysis, as well as characterization methods.

Renjie Chen is a Professor in the School of Materials Science and Engineering at Beijing Institute of Technology. His research focuses on electrochemical energy storage and conversion technology. He was a post-doctoral fellow in the Department of Chemistry at Tsinghua University and a visiting professor in the Department of Materials Science and Metallurgy at the University of Cambridge. As the principal investigator, Prof. Chen successfully hosted the National Key Research and Development Program of China, the National Natural Science Foundation of China, the National High Tech 863 project, etc. He has (co-) authored 335 research papers and filed over 50 patents and patent applications.

Wen Yang received his Ph.D. degree from Changchun Institute of Applied Chemistry, Chinese Academy of Sciences, in 2009. Following a brief stint at the Max Plank Institute of Colloids and Interfaces, he joined the Beijing Institute of Technology in 2011. In 2016, he worked as a tenure-track associate professor and was promoted to associate professor in 2021. His research interests focus on solid-state electrochemistry, including lithium-ion power batteries, solid-state lithium-ion batteries.